Title

Mitochondria dysregulation contributes to secondary neurodegeneration progression post-contusion injury in human 3D in vitro triculture brain tissue model.

Journal

Cell Death and Disease, 14(8)

Authors

Liaudanskaya, Volha
Fiore, Nicholas
Zhang, Yang
et al.

Publication Date

2023-08-03

DOI

10.1038/s41419-023-05980-0

CDDpress

www.nature.com/cddis

ARTICLE OPEN

Mitochondria dysregulation contributes to secondary neurodegeneration progression post-contusion injury in human 3D in vitro triculture brain tissue model

Volha Liaudanskaya[1], Nicholas J. Fiore[1], Yang Zhang[1], Yuka Milton[1], Marilyn F. Kelly[1], Marly Coe[1], Ariana Barreiro[1], Victoria K. Rose[1], Matthew R. Shapiro[1], Adam S. Mullis[1], Anna Shevzov-Zebrun[1], Mathew Blurton-Jones[2], Michael J. Whalen[3], Aviva J. Symes[4], Irene Georgakoudi[1], Thomas J. F. Nieland[1] and David L. Kaplan[1]✉

Traumatic Brain injury-induced disturbances in mitochondrial fission-and-fusion dynamics have been linked to the onset and propagation of neuroinflammation and neurodegeneration. However, cell-type-specific contributions and crosstalk between neurons, microglia, and astrocytes in mitochondria-driven neurodegeneration after brain injury remain undefined. We developed a human three-dimensional in vitro triculture tissue model of a contusion injury composed of neurons, microglia, and astrocytes and examined the contributions of mitochondrial dysregulation to neuroinflammation and progression of injury-induced neurodegeneration. Pharmacological studies presented here suggest that fragmented mitochondria released by microglia are a key contributor to secondary neuronal damage progression after contusion injury, a pathway that requires astrocyte-microglia crosstalk. Controlling mitochondrial dysfunction thus offers an exciting option for developing therapies for TBI patients.

Cell Death and Disease (2023)14:496 ; https://doi.org/10.1038/s41419-023-05980-0

INTRODUCTION

Traumatic brain injury (TBI) is a debilitating condition with multifaceted pathobiology that leads to long-lasting disabilities and morbidity. Primary TBI comprises direct injury to the brain and results in acute local neuronal death, excitotoxicity, and edema [1]. This complete and irreversible event triggers potentially preventable secondary injury that manifests in neuroinflammation, diffused axonal degeneration, and death of the surrounding tissue [2–4]. Astrocytes and microglia have dual roles in the progression of brain injuries [5, 6], promoting injurious inflammation and providing homeostatic and regenerative support [3, 6–8]. Mitochondria regulate glial activity and function through balanced mechanisms of fission and fusion that maintain their growth, shape, distribution, and structure [9]. Disruptions in mitochondrial function influence crucial pathways, such as activation of inflammation, energy production, metabolism, phosphorylation of transcription factors, and various death pathways regulation [10, 11]. Glial crosstalk has been shown to accelerate brain injury progression [12], where microglia trigger alterations in astrocytes characterized by increased secretion of pro-inflammatory factors, disrupted mitochondria function, and a failure to nurture neurons or eliminate foreign agents, which collectively leads to neurotoxicity and neuroinflammation [12, 13]. In neurodegenerative disorders such as Alzheimer's (AD), Parkinson's (PD), Huntington's disease (HD), and Amyotrophic lateral sclerosis (ALS), astrocytes were shown to be altered by fragmented extracellular mitochondria released from stimulated by the damage-associated molecular patterns (DAMP) microglia [14]. A key process in regulating mitochondria fragmentation is the phosphorylation of dynamin-related protein – 1 (Drp1) and its subsequent relocation to the mitochondrial outer membrane, which binds to the Fis1 receptor [10]. In rodent models of moderate types of brain injuries, blocking excessive Drp1-mediated mitochondria fission with an inhibitor of Drp1 catalytic activity (Mdivi-1) ameliorated early neuronal damage progression and improved behavioral outcomes [15].

While it is known that brain injury induces mitochondria dysregulation in rodents [15], and microglia-astrocyte crosstalk could be detrimental in neurodegenerative disorders [14], the role of glial mitochondria fragmentation to brain injury-induced secondary neurodegeneration remains to be established. Here we determined crosstalk and cell-type-specific contributions of neurons, microglia, and astrocytes to dysregulated mitochondria-driven neurodegeneration after moderate injury in a human 3D triculture tissue model of the brain. Our results demonstrated that microglia play a pivotal role in the progression of secondary damage post-contusion through increased pathological mitochondria fragmentation and its metabolic dysregulation.

[1]Department of Biomedical Engineering, Tufts University, Medford, MA, USA. [2]Department of Neurobiology and Behavior, University of California Irvine, Irvine, CA, USA. [3]Department of Pediatrics, Massachusetts General Hospital, Charlestown, MA, USA. [4]Department of Pharmacology and Molecular Therapeutics, Uniformed Services University, Bethesda, MD, USA. ✉email: david.kaplan@tufts.edu

Edited by Professor Michelangelo Campanella

Received: 7 December 2022 Revised: 13 June 2023 Accepted: 11 July 2023
Published online: 03 August 2023

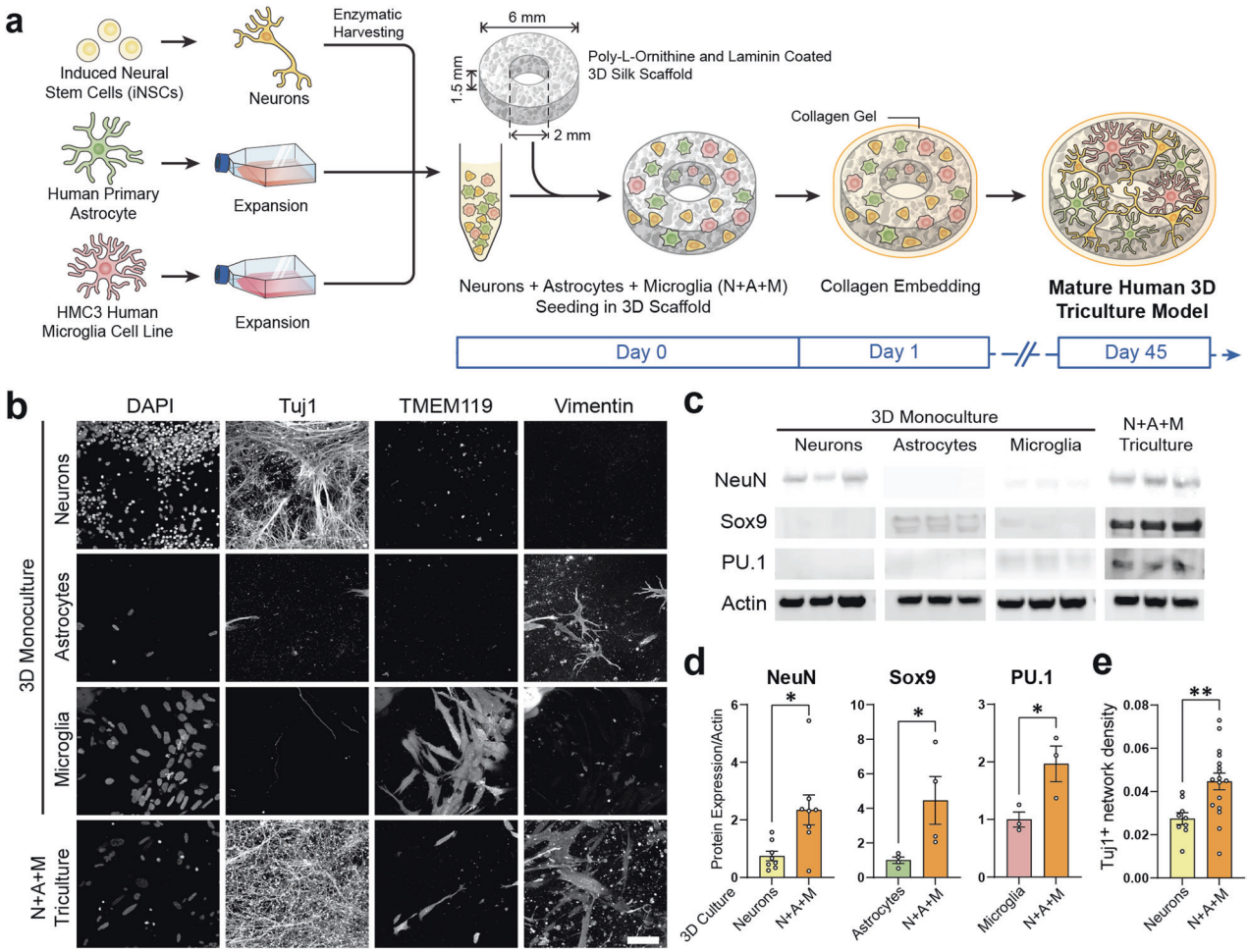

Fig. 1 Validation and characterization of human in vitro 3D triculture model composed of neurons, microglia, and astrocytes. **a** Schematic representation of the preparation of 3D tricultures. **b** Representative images of neuron (Tuj1), microglia (TMEM119), and astrocyte (Vimentin) specific cytoplasmic markers in monocultures and tricultures. **c** Representative images of Western blots stained with antibodies recognizing cell-specific transcription factors (NeuN (neuronal), Sox9 (astrocytic), PU.1 (microglial), or actin as a loading control. **d** Quantification of the Western blots showing results normalized to actin expression, and **e**, Tuj1 neuronal network density quantified from confocal z-stack images. Scale bar: 50 µm. **d** Means ± SEM of $n = 4$ scaffolds per condition. *, ** indicates a significant difference ($p < 0.05$, 0.01 respectively; t-test with Welch's correction was used to determine the differences between control and experimental groups). All experiments were replicated at least three times.

RESULTS

In vitro 3D human triculture brain tissue model fabrication and characterization

We developed a 3D in vitro triculture human tissue model of a contusion injury, composed of induced neural stem cells, human primary astrocytes, and an HMC3 microglia cell line (Figs. 1–5), or iPSC (induced pluripotent stem cells) derived microglia from two healthy donors (YZ1 and ND41866*C) (Figs. 6, 7). These human tricultures (neuron, astrocyte, and microglia culture (NAMc)) were generated by seeding neurons, astrocytes, and microglia at a ratio of 2:0.5:0.1 million, respectively, in 3D silk scaffolds and then enveloping them in a collagen type I hydrogel for sustained long-term growth (Fig. 1a, Supplementary Fig. 1-3, 21). Tri-cultures demonstrated upregulation of quintessential cell-type specific transcription factors (NeuN for mature neurons, Sox9 for astrocytes, and PU.1 for microglia) concomitant with an increase in density of beta-3-tubulin (Tuj1) positive neuronal networks (Fig. 1b–e, Supplementary Fig. 2-5), and its homeostatic state was confirmed through analysis of inflammatory markers (Supplementary Fig. 6). Moreover, additional characterization of the cellular state in tricultures was performed using RNA sequencing analysis (Supplementary Fig. 4, 5).

A selective inhibitor of excessive mitochondrial fragmentation blocks injury-induced neuronal network degeneration

The 3D cultures were exposed to P110 peptide, a selective inhibitor of DRP1 GTPase activity without affecting the activity of fusion proteins (OPA1 mitochondrial dynamin-like GTPase (OPA1) and mitofusin 1 (MFN1)) [16]. Human 3D tri-, di-, and mono-cultures were subjected to contusion injury using a controlled cortical impactor (CCI, here and after "CCI" in figures refers to the model of induced injury) at 45-50 days post-seeding, using parameters established previously in vitro and in vivo (Fig. 2b, c, Supplementary Fig. 7-11) [17].

In neuronal culture (Nc), neuron + astrocytes culture (NAc), and neuron + microglia culture (NMc), the neural network in the directly impacted area (Supplementary Fig. 8) degraded by 90% within 24 h ($p < 0.01$) in the absence or presence of P110. In NAMc, we observed intact neuronal network density in the directly impacted area within 24 h in P110 treated group but not the control (Supplementary Fig. 8-9). In the adjacent to the injury site, of the neuronal monocultures, network density declined from 24 h up to 14d after the injury (from 50% degeneration at 24 h and 48 h to 60% at 14d, $p < 0.01$) (Fig. 2d, e; Supplementary Fig. 10). In contrast, NAc or NMc showed (90%) network survival after injury,

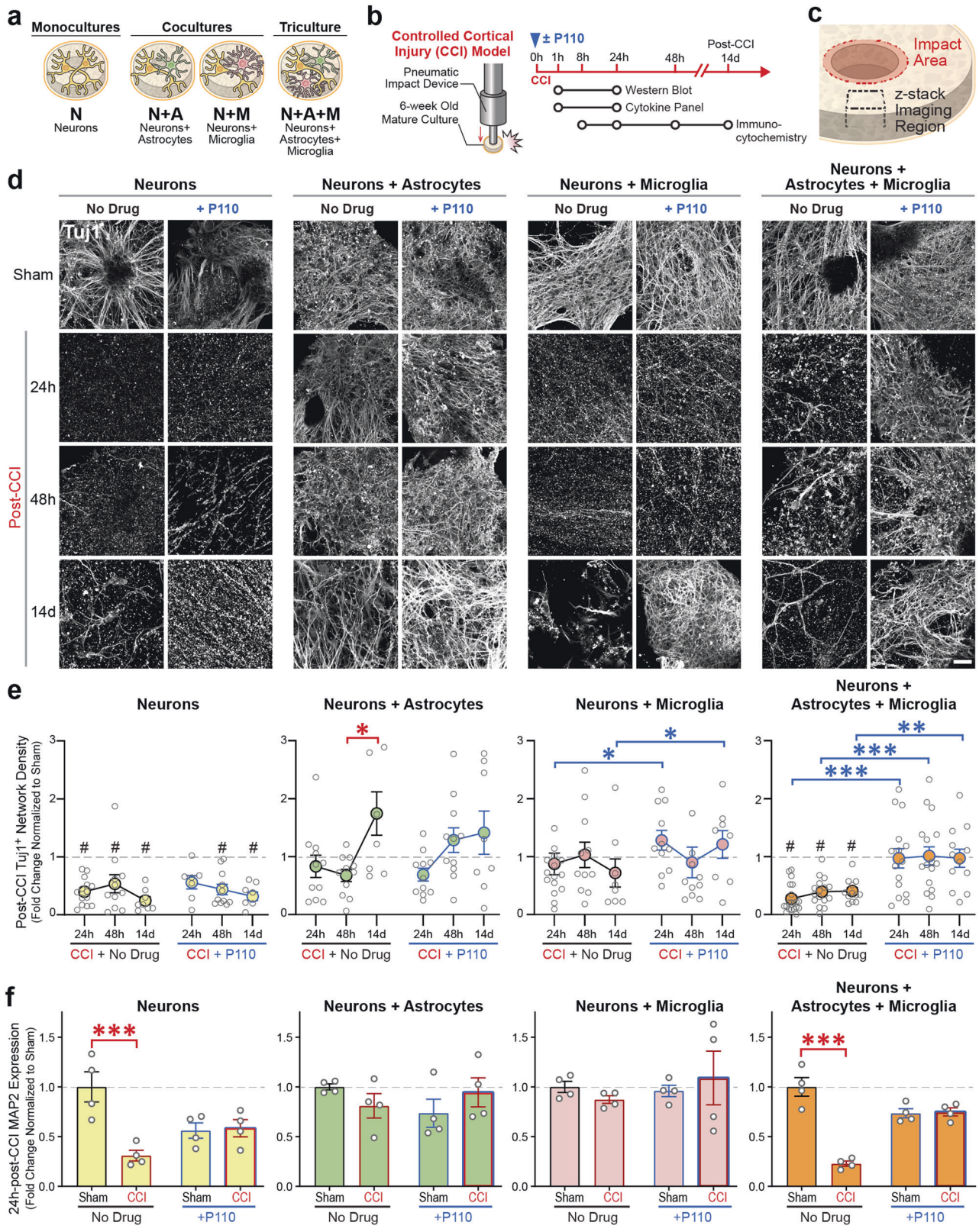

up to 48 h, that decreased by 30% in NMc at 14d. Injured NAMc showed 80% drop in network density at 8 h after the impact, and it remained 70-80% degraded for up to 14d ($p < 0.05$). With P110 treatment, the network was preserved in the NA, NM, and NAM cultures at all time points. However, in Nc, the drug protected the network from degradation compared to sham only at the 24 h time point (Fig. 2d, e; Supplementary Fig. 10). There was no difference compared to injured samples without drug treatment. The above results were corroborated with Western blot analysis of MAP2 protein, the dendritic marker of mature neurons, 24 h after

Fig. 2 Neuronal network degeneration in tricultures with microglia and astrocytes, but not neuronal monocultures, is reversible with mitochondria fission inhibitor P110. a Schematic representation of experimental groups. **b** Contusion (Controlled cortical impact model (CCI)) injury experimental design. **c** Schematic representation of the injury area, and image acquisition. **d** Representative images of Tuj1 neuronal staining at 24 h, 48 h, and 14d after injury in N, NA, NM, and NAM groups. **e** Quantification of Tuj1 neuronal network density in control and P110 treated groups of N, NA, NM, and NAM at three different time points (24, 48 h, and 14d). **f** Quantification of MAP2 protein Western blots at 1 h and 24 h after injury in all groups. Proteins were isolated from entire scaffolds without separating the injured area from the penumbra. Data presented in **e** and **(f)** mean ± SEM of three independent experiments with $n = 3$ for sham groups and $n = 4$ scaffolds for injury groups. *, **, *** indicate significant differences ($p < 0.05$, 0.01, 0.001 respectively; two-way ANOVA (analysis of variance) (with Tukey's post-hoc test) between control and experimental groups). Scale bar: 50 µm.

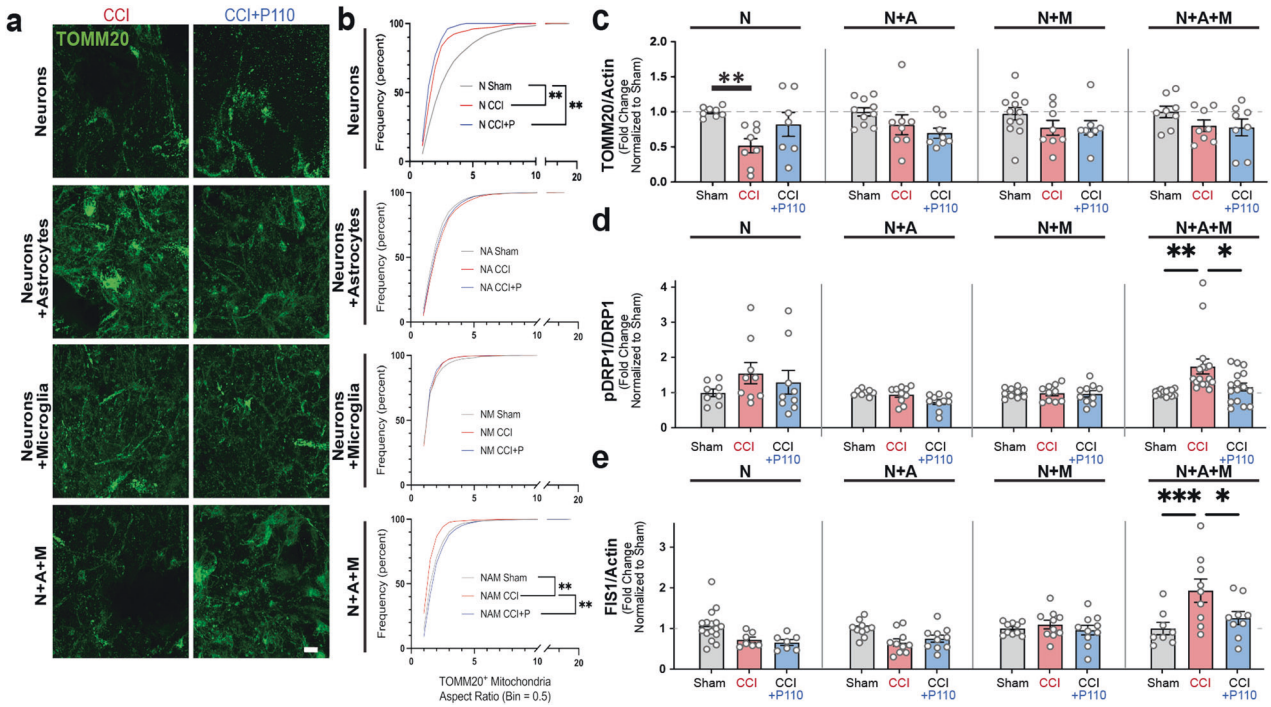

Fig. 3 Injury-induced neurodegeneration in tricultures, but not neuronal monocultures, was associated with increased Drp1-Fis1 driven mitochondria fission. a Representative images of TOMM20 mitochondria at 24 h after contusion in N, NA, NM, and NAM groups. **b** Frequency distribution (%) of TOMM20-positive mitochondria aspect ratio in control and P110 treated groups of N, NA, NM, and NAM. **c** TOMM20 protein quantification by Western blot 24 h after injury in all groups. **d, e** pDRP1/DRP1, and Fis1 protein quantification by Western blot 24 h after the injury in all groups. Proteins were isolated from entire scaffolds without separating the injured area from the penumbra. Data presented in **(b-e)** mean ± SEM of three independent experiments with $n = 3$ for sham groups and $n = 4$ scaffolds for injury groups. *, **, *** indicates significant difference ($p < 0.05$, 0.01, 0.001 respectively; two-way ANOVA (with Tukey's post-hoc test) between control and experimental groups).

injury (Fig. 2f, Supplementary Fig. 11). A reduction of MAP2 was observed in Nc and NAMc conditions (60% drop, $p < 0.01$), with unchanged levels in the P110 group.

Next, we confirmed necroptotic pathway activation [18] in Nc and NAMc through phosphorylation of mixed lineage kinase (pMLKL) (Supplementary Fig. 12) while phosphorylated receptor-interacting serine/threonine-protein kinase 3 (pRIP3) was not detected. At last, the P110 peptide had no significant effect, indicating that P110 acts downstream of necroptosis activation.

Neuronal network degradation is associated with mitochondrial fission

To confirm that mitochondria fission was associated with neuronal network degeneration, the mitochondria aspect ratio (AR, a measure of mitochondria width over length; Fig. 3a, b), the total amount of TOMM20 (translocase of outer mitochondrial membrane 20) mitochondria, and the expression levels of fission (Fig. 3c–e, Supplementary Fig. 13) and fusion markers (Supplementary Fig. 14) were analyzed. Nc showed a decreased amount of TOMM20-positive mitochondria with a high fragmentation rate 24 h after injury, partially rescued in the presence of the P110 peptide, unlike the AR. In control or P110-treated injured NMc, NAc, and NAMc, there was no decline in the amount of TOMM20-positive mitochondria (Fig. 3c). In the injured NAc and NMc with/without P110 treatment, the AR and mitochondria fission and fusion levels remained equal to shams. While the total amount of mitochondria remained unchanged in NAMc, the mitochondria underwent a significant transition to the fragmented state after injury, showing a decreased mitochondria AR and increased expression of pDRP1 (dynamin-related protein-1 phosphorylated at Serine 616) and Fis1 (mitochondria fission one protein), two factors responsible for mitochondria fission, but not fusion proteins (Fig. 3, Supplementary Fig. 13-14). Mitochondria fragmentation was reversed in the P110 treated tricultures (NAMc), showing sham levels of pDRP1 (Fig. 3d) and Fis1 expression (Fig. 3e), and sham level of aspect ratio (Fig. 3a, b).

Increased mitochondria fission is associated with neuroinflammation

We next evaluated if mitochondria fragmentation influenced acute neuroinflammation in NAM tricultures 24 h after the injury (Fig. 4, Supplementary Fig. 15). Increased expression of disease-associated

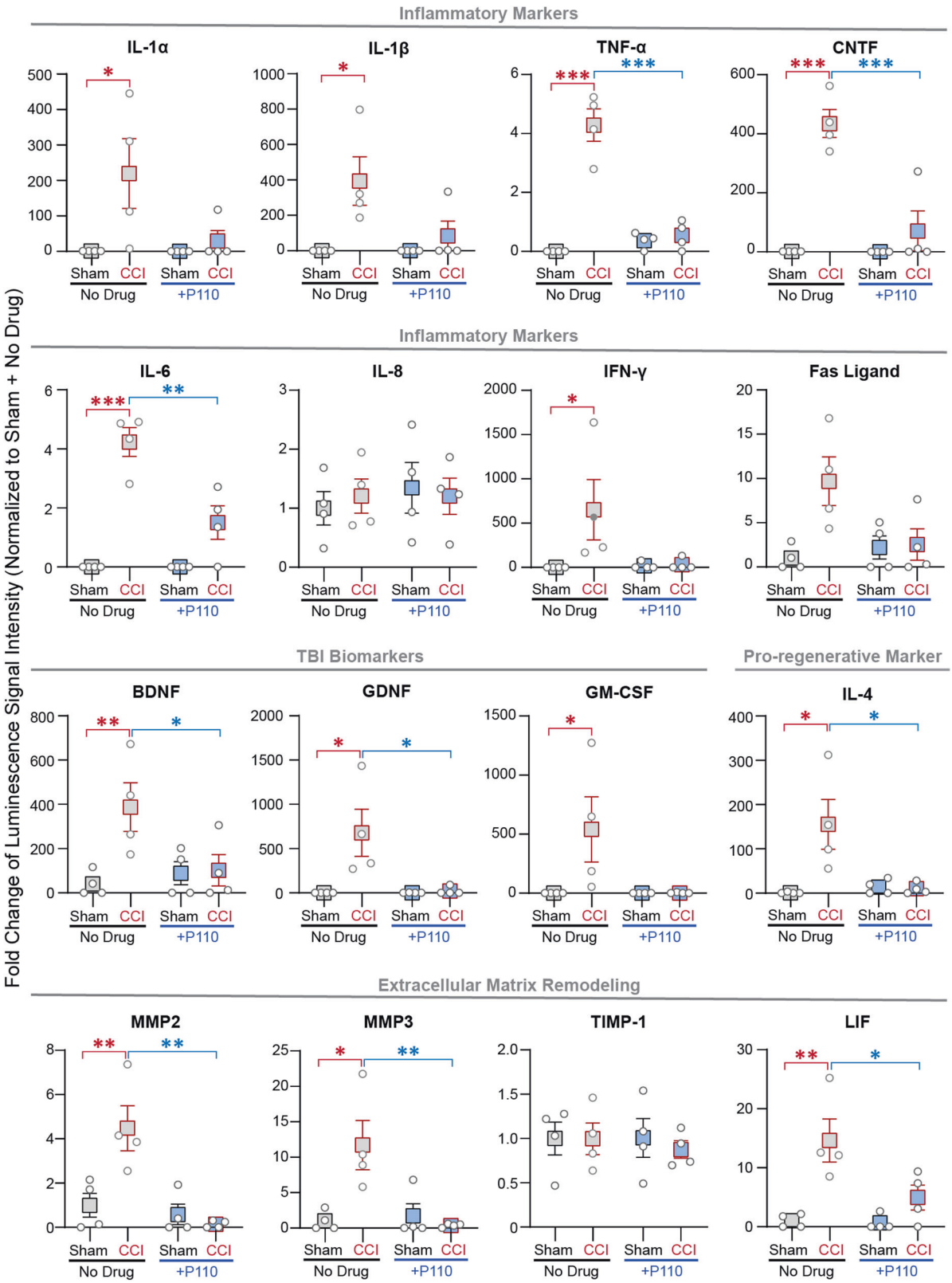

Fig. 4 Increased secondary neurodegeneration was associated with neuroinflammation in tricultures 24 hours after injury. Human Neuro Discovery Array of inflammatory markers: IL-1α, IL-1β, TNFα, CNTF, IL6, IL8, IFNγ, and Fas ligand; Neurotrophic and Growth factors: BDNF, GDNF, GM-CSF; Pro-regenerative marker: IL-4; Extracellular matrix remodeling proteins: MMP2, MMP3, LIF, and TIMP1 secreted 24 h after injury in triculture NAM cultures with/-out P110 treatment. Data normalized to sham without drug treatment. Data presented are the mean ± SEM of four independent experiments, with each data point being the average for $n = 4$ scaffolds per condition. *, **, *** indicate significant differences ($p < 0.05$, 0.01, 0.001, respectively; two-way ANOVA (with Tukey's post hoc test) between control and experimental groups).

markers [12, 14, 19] interleukin-1 alpha, beta (IL-1α, IL-1β), tumor necrosis factor-alpha (TNFα), and ciliary neurotrophic factor (CNTF) was mitigated in the presence of P110 after injury. Additionally, C-C motif chemokine ligand 2 (CCL2), interleukin-6 (IL-6), interferon-gamma (IFNγ), and other acute inflammatory markers (Supplementary Fig. 15) were upregulated after injury and mitigated with P110 treatment. TNF-α and Fas ligand (FasL) has been linked to worsened outcomes after CCI in mice and proposed as contributors to secondary damage progression [20]. Here, we found upregulated expression of both TNFα and FasL, which was rescued with P110

Fig. 5 Mitochondria dysregulation in microglia was crucial for secondary neurodegeneration and neuroinflammation progression post-contusion injury. a Schematic representation of transfer experiment from neurons to microglia to astrocytes, and neurons with/without P110 compound performed at each transfer step. Representative images of **b**, Tuj1, and **d**, TOMM20 staining of naïve neurons treated for 24 h with mitochondria isolated from astrocytes activated with mitochondria isolated from microglia that were treated with conditioned media collected from 24 h injured neurons with quantification of **c**, Tuj1 positive neuronal network density, and **e** TOMM20 positive mitochondria aspect ratios. **f** Quantification of the pDRP1/DRP1 and Fis1 proteins expression in N-M-A-N control and P110 treated groups. **g** Inflammatory cytokine secretion in N-M-A-Nt control and P110 treated groups. **h**, Schematic representation of the metabolic image analysis. **I** Representative redox ratio maps of mitochondria isolated from microglia activated by conditioned media from injured neurons. Quantification of **j**, redox ratio, **k** NADH bound fraction, and **l**, a long lifetime in live mitochondria isolated from microglia, astrocytes, and neurons treated with mitochondria isolated from injured neurons, activated microglia, or astrocytes. Proteins were isolated from entire scaffolds without separating the injured area from the penumbra. Data presented in **(c, e, f, g, j, k, l)** mean ± SEM of three independent experiments with $n = 3$ for sham groups and $n = 4$ scaffolds for injury groups. *, **, ***, **** indicates significant difference ($p < 0.05$, 0.01, 0.001, 0.0001 respectively; one-way or two-way ANOVA (with Tukey's post hoc test) between experimental groups). Experiments were replicated at least three times; metabolic images were replicated two times. Scale bar in **b**, **d:** 50 µm; in **i:** 10 µm.

treatment. Some TBI biomarkers, such as brain-derived neurotrophic factor (BDNF), glia cell-derived neurotrophic factor (GDNF) [21], granulocyte-macrophage colony-stimulating factor (GM-CSF) [22], and S100 calcium-binding protein B (S100B) [23] were upregulated after injury, and the response was mitigated in the presence of P110 (Fig. 4, Supplementary Fig. 8).

The brain changes the extracellular environment after injury [7]. Here we found an increase in matrix metalloproteinases-2 and -3 (MMP2 and MMP3) with the injury and mitigated with P110 treatment, while tissue inhibitors of metalloproteinases (such as TIMP1) remained unchanged in the control and P110 group (Fig. 4). Some TBI markers, such as interleukin-8, -18 (IL-8, IL-18), vascular endothelial growth factor (VEGF) and T-cell directed CC Chemokine (TARC) remained unchanged in response to contusion or the presence of P110 (Fig. 4, Supplementary Fig. 15) [24]. Some known pro-regenerative markers such as interleukin -4, -10 (IL-4, IL-10), and transforming growth factor beta (TGFβ) were upregulated after contusion but remained at sham levels in the P110 group. Together, these results indicated that mitochondria fission regulates neuroinflammation post-injury.

Dysfunctional mitochondria contribute to injury-induced neurodegeneration and neuroinflammation

We further investigated the cell-specific contributions of mitochondria dysregulation to secondary damage progression post-injury (Fig. 5a–g; Supplementary Fig. 16). Conditioned media (CM) or mitochondria from injured neurons were not sufficient to induce neurodegeneration after transfer to naïve neuronal monocultures (N-N transfer; N-Nt) (Supplementary Fig. 16); if CM from injured neurons was transferred to naïve microglia, and then extracellular mitochondria from these cultures were added to naïve Nc, we observed about 50% of network degradation ($p < 0.05$; N-M-Nt) (Supplementary Fig. 16c, d). This effect was exacerbated by 75% of network degradation ($p < 0.01$; N-M-A-Nt, please see Fig. 5a for the schematic of the experiment) when naïve neurons were treated with mitochondria isolated from astrocyte cultures (that were treated for 24 h with extracellular mitochondria from microglia, activated by CM from injured neurons) (Fig. 5b, c). Increased network degeneration was concomitant with a significant drop in mitochondria aspect ratio (Fig. 5d, e). To evaluate a cell type-specific contribution to injury progression, NAc were treated with dysfunctional mitochondria released from activated microglia and NMc with astrocytic mitochondria (Supplementary Fig. 17). We observed neuronal network degeneration only in NAc treated with mitochondria from microglia and the degeneration was prevented with P110 treatment (Supplementary Fig. 15).

To further examine the role of crosstalk between astrocytes and microglia in mitochondrial-induced neurodegeneration, we focused on the injured neuron to microglia to astrocyte to neuron transfer (N-M-A-Nt); please see Fig. 5a for experimental design. Besides damaged axonal (Fig. 5b, c) and mitochondria networks (Fig. 5d, e), we observed induction in pDRP1 and Fis1-associated mitochondria fission (Fig. 5f), restored with P110 treatment. Next, we detected elevated expression of pro-inflammatory markers IL-1α, IL1-β, IL-6, IFN-γ, TNF-α, FasL, MMP2, and MMP3 (Fig. 5g, Supplementary Fig. 18), mitigated in the presence of the P110 peptide. We thus confirmed the contribution of extracellular mitochondria to fission-associated secondary neurodegeneration and neuroinflammation progression in neurons after brain injury (Fig. 5a–f).

We next characterized the function of mitochondria released by neurons, astrocytes, and microglia in transfer experiments (N-M-A-Nt) (Supplementary Fig. 19-20). Activated microglia and astrocytes in a fission-dependent manner released more mitochondria with decreased ATP production and oxygen consumption levels. The number of mitochondria released by activated naïve neurons was not different from the sham; however, with a lower ATP production rate and increased oxygen consumption. P110 treatment induced increased secretion of mitochondria with a lower oxygen consumption rate.

We next used real-time imaging of isolated mitochondria to assess metabolic function based on the endogenous two-photon excited fluorescence of NAD(P)H (reduced nicotinamide adenine dinucleotide (phosphate)) and FAD (flavin adenine dinucleotide). The intensity images were used to calculate the redox ratio, defined as FAD/(NAD(P)H + FAD), while lifetime images were analyzed to extract the fraction of NAD(P)H in bound form and it's corresponding (long) lifetime (Fig. 5h–l) [25]. Extracellular microglial mitochondria showed an increased redox ratio following injury, mitigated with P110 treatment (Fig. 5i, j); in astrocytic mitochondria, the redox ratio remained at the sham level in both control and P110 groups (Fig. 5j), while neuronal mitochondria showed a significant drop in redox ratio after injury in the untreated group and increase in P110 treated group (Fig. 5j). The bound fraction of NADH was consistently lower in P110 treated astrocytes and neurons (Fig. 5k). In the injury group, it was lower only in neurons, and no change was observed in the microglia group. The long NAD(P)H lifetime was lower in the P110 group in astrocytes and neurons (Fig. 5l), and for the untreated injury group only in neurons (same as what was observed with bound fraction measurement); no change was detected in microglia following contusion injury with or without P110 treatment. Our data demonstrated that extracellular mitochondria derived from microglia, activated by conditioned media from injured neurons, are dysfunctional and trigger a cascade of metabolic changes in astrocytic and neuronal mitochondria.

Mitochondria-induced neurodegeneration is independent of the microglia cell source

To test if the fragmented mitochondria-driven neurodegeneration is inherent to microglia and not just the HMC3 cell line, we replicated the experiments with iPSC-derived microglia from two healthy donors (YZ1 and ND41866*C) (Figs. 6, 7, Supplementary Fig. 21-33), and further characterized the genetic response of 3D in vitro tricultures to contusion injury, using mRNA sequencing analysis. Microglia were differentiated following an established

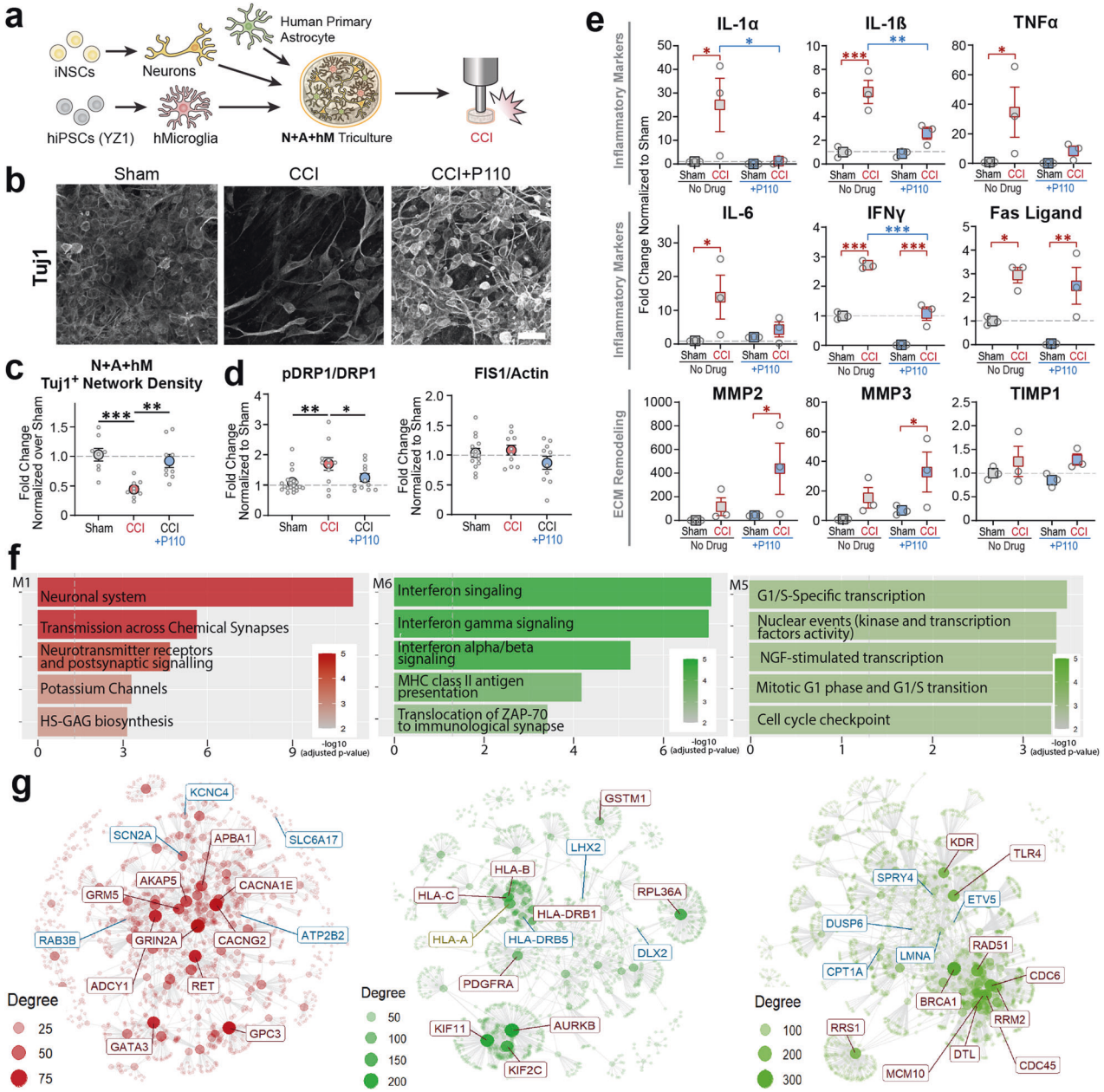

Fig. 6 Dysfunctional mitochondria released from iPSC-derived microglia (YZ1 line from a healthy donor) induced neurodegeneration and neuroinflammation progression 24 hours after contusion injury. **a** Schematic representation of the experimental design. **b** Representative images of Tuj1 network density in tricultures with iPSC-derived microglia. **c** Quantification of the Tuj1 neuronal network density in control and P110 treated groups of NAMc. **d** Mitochondria fission associated pDRP1 and FIS1 proteins expression in control and P110 treated NAM cultures. Proteins were isolated from entire scaffolds without separating the injured area from the penumbra. **e** Inflammatory cytokines secretion post-injury in YZ1 triculture groups. **f** Gene set enrichment analysis revealed distinct expression modules associated with M1 - neuronal systems (negatively associated with a contusion in CTRL; rescued with P110); M5 - replication and repair (positively associated with a contusion in CTRL and P110); M6 - interferon signaling (positively associated with a contusion in CTRL; unchanged in P110). **g** Critical regulators of molecular mechanisms associated with M1, M5, and M6 modules. The full map of 7 detected modules and corresponding pathways can be found in Supplementary Fig. 25, 26, and 29. Data presented in **(c, d, e)** mean ± SEM of three independent experiments with $n = 3$ for sham groups and $n = 4$ scaffolds for injury groups. Data presented in **(f, g)** were analyzed from mRNA sequencing data collected from $n = 6$ for sham groups and $n = 6$ scaffolds for injury groups from two independent experiments. *, **, *** indicates a significant difference ($p < 0.05$, 0.01, 0.001 respectively; two-way ANOVA (analysis of variance) or one-way ANOVA between control and experimental groups) (with Tukey's post-hoc test). Experiments were replicated at least three times. Scale bar: 50 μm in **b, f, h**; 10 μm in **j**.

protocol [26, 27] and characterized for specific marker expression after each round of differentiation (Supplementary Fig. 21). We prepared 3D triculture tissues with iPSC-derived microglia following the protocol described above (Fig. 1, Supplementary Fig. 1-6) and performed viability staining at specific timepoints to ensure healthy, symbiotic growth of the three cell-types in NAMc (Supplementary Fig. 22). After 6 weeks, the 3D tricultures went through the injury protocol, and the effect of contusion injury was observed after 24 h (Fig. 6; Supplementary Fig. 23-33). The neuronal network degraded in mitochondria fission-dependent manner by 50% ($p < 0.05$) in cultures containing microglia cells from either donor, and the effect was reversed in the presence of

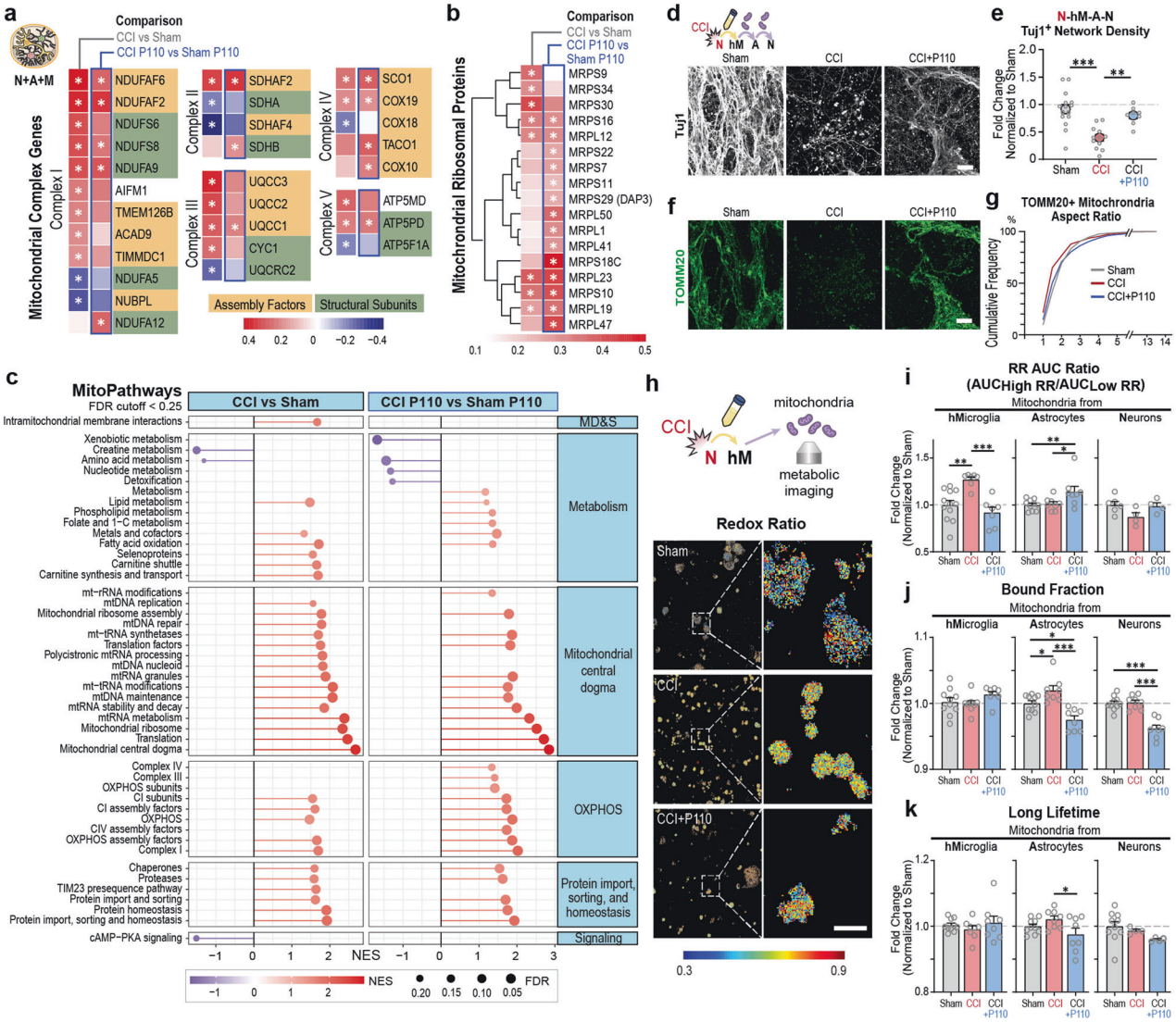

Fig. 7 Contusion injury-induced dysregulation of intra- and extracellular mitochondria. Differentially expressed genes (DEGs) associated with **a**, mitochondria complex genes; and **b**, mitochondria ribosomal proteins were detected (abs(Log2(Fold Change))> 0.585 and q < 0.01) in human 3D in vitro triculture model composed of induced neural stem cells derived neurons, primary astrocytes, and iPSC-derived microglia from two healthy donors YZ1 and ND41866*F ($n = 6$) and summarized in the over-representation analysis of **c**, mitochondria pathways. **d, f** Representative images, and **e–g** quantifications of Tuj1 neuronal and TOMM20 mitochondria networks in naïve neurons treated with mitochondria isolated from astrocytes activated with mitochondria isolated from YZ1 microglia that had been treated with conditioned media collected from 24 h injured neurons. **h**, Representative redox ratio maps of mitochondria isolated from microglia activated by conditioned media from injured neurons. Quantification of **i**, redox ratio, **j**, bound fraction, and **k**, a long lifetime in live mitochondria isolated from iPSC microglia, astrocytes, or neurons following N-M-A-Nt experimental design (Fig. 5a). Data presented in **(a–c)** were analyzed from mRNA sequencing data collected from $n = 6$ for sham groups and n = 6 scaffolds for injury groups from two independent experiments. Data presented in **(e, g, i–k)** mean ± SEM of $n = 6$–10 scaffolds per condition. *, **, *** indicates a significant difference ($p < 0.05$, 0.01, 0.001 respectively; two-way ANOVA (analysis of variance) or one-way ANOVA between control and experimental groups) (with Tukey's post hoc test). Experiments were replicated at least three times, unless otherwise specified; metabolic images were replicated two times. Scale bar: 50 μm in **d, f**; 10 μm in **h**.

P110 (Fig. 6a–c; Supplementary Fig. 23a-c, 24). Similar to HMC3 tricultures (Figs. 4, 5), we observed mitochondria fission-induced neuroinflammation (IL-1α, IL-1β, and TNFα) (Fig. 6e, Supplementary Fig. 25, 26). Please see supplementary information for Fig. 6 provided before Supplementary Fig. 1.

Contusion injury induced mitochondria intra- and extracellular changes in human 3D triculture model of brain injury

mRNA expression analysis of mitochondria-specific markers detected increased expression of genes associated with mitochondria oxidative phosphorylation (OXPHOS, complex I and III), while P110 treatment mitigated the increase in some of these markers (Fig. 7a). Next, mitochondria ribosomal protein genes were upregulated in the P110 treated group (Fig. 7b) compared to control injury or sham groups. Further, a significant downregulation of glycolysis genes was observed in control and P110 groups (Supplementary Fig. 32), together with the mitochondria metabolism of creatinine and amino acids genes. At last, increased expression of carnitine metabolism genes was detected, potentially providing an alternative path for NADH generation for the OXPHOS pathway [28].

To confirm microglial mitochondria fission contribution to neurodegeneration, the transfer experiments were replicated in iPSC microglia-based models (Fig. 7d–k; Supplementary Fig. 23e, f; 33). Extracellular mitochondria isolated from astrocytes (please see Fig. 5a for experimental design) induced neurodegeneration in cultures with

ND41866*C line to 75% of network degradation (N-M-A-Nt; Supplementary Fig. 23e, f) and to 50% with YZ1 line (Fig. 7d–g). These effects were associated with increased levels of mitochondria fragmentation in both lines (Fig. 7f, g; Supplementary Fig. 23 e, f).

We next examined the metabolic profile of mitochondria released from neurons, astrocytes, and iPSC microglia (YZ1 line) after exposure to conditioned media from injured neurons (Fig. 7h–k; N-M-A-Nt). We observed an increased level of redox ratio in microglial mitochondria, rescued with P110 treatment, an increased signal in the P110 astrocytes group, and no change in the neurons (Fig. 7i). The NADH bound fraction was consistently lower in P110-treated astrocytes and neuronal groups, with no changes in the microglia group (Fig. 7j). Together these findings confirmed cell-line independent effects of microglial mitochondria fission on secondary neurodegeneration and neuroinflammation progression after contusion injury.

DISCUSSION

The temporal profile of neuroinflammation and neurodegeneration after brain injury has been studied in animal models of TBI and in brain tissue, cerebrospinal fluid, and plasma samples from TBI patients [5]. While rodent models help explore behavioral changes and multicellular interactions between the central and peripheral nervous systems, limitations include innate differences between rodents and humans (such as white/grey matter ratio, microglia activation early after TBI in rats vs. persistence for years in humans, genetics) [29], screening limits due to animal use and costs, and the lack of options for long-term studies (years). Human clinical samples are useful for detecting biomarkers and understanding late stages of disease progression; however, they cannot be used to study molecular triggers and disease onset or to perform exploratory research of underlying mechanisms. To overcome these limitations, we developed a preclinical human 3D in vitro model consisting of multiple neural cell types (neurons, astrocytes, and microglia) for studying cell-specific contributions to injury progression. The engineered tissues withstand the mechanical insult and recapitulated TBI primary injury hallmarks [1, 30–32], such as progressive neuronal network damage (Figs. 2, 6; Supplementary Fig. 7-10, 23), glutamate release (Supplementary Fig. 7), increased membrane permeability, as witnessed by LDH release into the media (Supplementary Fig. 7), and secretion of inflammatory and neurotrophic factors (IL-1α, IL-1β, IL-6, TNF-α, BDNF, NGF, as well as others) (Figs. 4, 6; Supplementary Fig. 15, 23, 25-26).

In vivo and human studies suggest that increase in glycolysis (e.g., short-term (12 h), followed by prolonged glycolytic depression (up to a few weeks) [33] and decrease in the oxygen metabolism through oxidative phosphorylation cycle in the long-term (weeks) [34, 35]) lead to brain tissue loss and poor behavioral outcomes (e.g., spatial and motor learning, anxiety, fear, activity) in moderate and severe TBI [36]. In this study, we observed neurodegeneration progression in neuronal monocultures that was accelerated in tricultures, suggesting a toxic gain-of-function of glial cells. The underlying mechanisms of injury-induced neurodegeneration partly depend on mitochondria acquiring a pathological state characterized by excessive fission that can be rescued by a specific inhibitor (P110). Next, we detected decreased expression of glycolysis-associated genes; however, further experiments are required to confirm if glycolysis is compromised. Intriguingly, despite decreased glycolysis level, the expression of genes associated with OXPHOS was increased 24 h after the injury, potentially using pyruvate produced through the increased carnitine metabolism or fatty acid oxidation.

At last, rodents and 2D in vitro models linked fragmented mitochondria with the progression of several neurodegenerative disorders and the TBI [14, 15]. In 2D models of ALS, AD, PD, and HD, these effects can be mimicked in neural cell cultures by exposure to mitochondria released from the glia [14]. However, the link between cell-specific mitochondria dysregulation to neuronal damage has never been shown in TBI. Our results indicated that mitochondria released from activated microglia (cell line or iPSC-derived) were a driving force of secondary neural damage progression (N-M-Nt). The mechanism of mitochondrial release and the factors released by injured neurons to stimulate microglia remain to be characterized but could involve active signaling, dying cells, and DAMPS [14, 37]. In transfer experiments including astrocytes (N-M-A-Nt), induction of mitochondria fission and neuroinflammation was coupled to accelerated neurodegeneration, suggesting a feedback loop of injury-induced damage progression and crosstalk between the three cell types. Label-free, optical assessments of mitochondrial metabolism suggest that extracellular microglial mitochondria shift to a more oxidized state, possibly as a result of oxidative stress (Fig. 5h–l and 7h–k) [38–40]. In P110-treated astrocyte and neuronal groups, the combined decrease in the NAD(P)H bound fraction and long lifetime in extracellular mitochondria may be attributed to enhanced utilization of NADPH in the glutathione pathway to combat injury-induced oxidative stress [41].

A major advantage of our bioengineered 3D tissues over other in vitro models (e.g., 2D cultures, brain-on-chip) is the ability to inflict physiologically relevant mechanical injuries and monitor the primary and secondary injury progression over an extended time frame [42]. Cells in this 3D system remain functional for over 2 years, providing opportunities to understand cellular and genetic contributions to injury progression and pharmacological interventions [43, 44]. The key finding of the present TBI study is the pivotal role of glial-neuronal crosstalk in the progression of secondary damage and neuroinflammation and the role of mitochondria function therein. These data suggest that selective inhibition of pathological mitochondrial fission mediated by Drp1-Fis1 could be a potential therapeutic target for TBI patients.

MATERIALS AND METHODS

3D silk scaffold preparation

Silk processing and scaffold fabrication. Silk scaffolds were prepared from silk fibroin following a previously established protocol (Rockwood et al., 2011). *Bombyx mori* cocoons were boiled for 30 minutes in a sodium carbonate solution (0.02 M) to isolate silk fibroin and remove sericin. The fibroin fibers were dried overnight in a fume hood. The following day, the silk fibers were dissolved in 9.3 M lithium bromide (Sigma) by immersion for 4 h at 60 °C. Dialysis of the silk in deionized water at room temperature was performed for 3 days in 3,500 molecular weight cut-off dialysis tubing (Invitrogen) to remove the lithium bromide from the silk. The resulting silk solution was centrifuged twice at 9,000 rpm for 20 minutes, and a strainer with 100 µm pores was used to filter out the remaining debris. Then, 1 mL of the silk solution was dried at 60 °C overnight to determine the weight/volume (w/v) concentration. The silk solution concentration was adjusted to 6 mg/mL and combined in a 10 cm dish with 400 to 500 µm sodium chloride (Sigma) particles at a ratio of 1:2 (v/w) and left for 2 days at room temperature to trigger pore formation and crystallization for stability in aqueous solution and to further refine the 3D sponge structures; the solution was incubated for one hour at 60 °C. After separating the sponge from the dish, residual sodium chloride was removed by dialysis in deionized water for 2 days at room temperature with 6 water changes total. The sponges were cut into individual donut-shaped scaffolds using biopsy punches (Integra) with a 6 mm outside and 2 mm inside diameter. The scaffolds were trimmed to a height of 1.5 mm using scissors and a razor blade. Scaffolds were then autoclaved in excess deionized water for 20 minutes with the liquid cycle, cooled to room temperature, and then processed for coating as described below. Silk scaffolds were used for experiments within 3-months of preparation.

Coating silk scaffolds with extracellular matrix. Scaffolds were coated with 10 µg/mL poly-ornithine (PLO) (Sigma, cat.no. A004C) and 5 µg/mL laminin (Fisher, cat. no. 501003381) to aid in cell adhesion. Up to 50 scaffolds were placed in a single well of a 6-well plate using fine forceps and incubated overnight at 37 °C in 7 ml of a 10ug/ml PLO coating solution in distilled water. The next day, the PLO was aspirated and washed three times with PBS with 5-minute incubations between washes. The scaffolds were then incubated

overnight at 4 °C in 0.5 mg/mL 100µL laminin stock aliquots with Dulbecco's Modified Eagle Medium/Nutrient Mixture (DMEM/F12, Invitrogen) phenol red-free media (PRF) in a 1:100 ratio and then the scaffolds were retained in the laminin solution. The scaffolds were incubated at 37 °C for 3 h before use.

Cell culture

Mycoplasma testing. All cell lines used in this project were tested for Mycoplasma at the Charles River Research Animal Diagnostic Services every 4-6 months.

Mouse embryonic fibroblasts (MEFs). Following ATCC guidelines, MEFs were used as a feeder layer for induced neuronal stem cells. MEFs were used at passages 1-3. DMEM (Invitrogen) supplemented with 10% Fetal Bovine Serum (FBS) (Invitrogen), and 1% Antibiotic-antimycotic (Anti-Anti) (Invitrogen) were used to maintain the MEFs. The media was changed every 3 days. Cells were passaged at 80% confluency. In brief, cells were washed with PBS and then treated with 0.25% Trypsin-EDTA solution for 3 min at 37 °C. Once the Trypsin-EDTA (Invitrogen) was deactivated with MEF media, the cells were centrifuged for 5 min at 1000 rpm. The MEFs were further split from 1 dish into 3 dishes (15cm^2).

As a feeder layer, the MEFs were allowed to reach 100% confluency and then inactivated with 10 µg/mL Mitomycin C (Sigma, M4287) for 3 h, followed by three washes with PBS. After the last PBS wash, media was added to the plates, and the cultures were maintained until the hiNSC seeding (7 days maximum).

Induced human neural stem cells (hiNSCs). The hiNSC cell line was previously generated from dermis-derived human fibroblasts, isolated from human neonatal foreskin fibroblasts through direct reprogramming [45]. hiNSCs were handled following a previously established protocol [3]. The cells were maintained in media composed of KnockOut DMEM (Invitrogen) supplemented with 1% GlutaMax (Invitrogen); 20% KnockOut Serum Replacement (Invitrogen); 1% Anti- Anti (Invitrogen); 0.2% β-mercaptoethanol (Invitrogen); 800 µL of 10 µg/mL basic fibroblast growth factor (Invitrogen) added proportionally to aliquots of media upon use. Media was changed daily. In brief, hiNSCs were expanded and subcultured on top of inactivated mouse embryonic fibroblasts. When cells reached 70–80% confluency, they were lifted from the plates via incubation with TrypLE solution for 1 min at 37 °C, followed by quenching with 6 mL of hiNSCs expansion media. Cells were then collected and pelleted by centrifugation at 3000 rpm for 2 minutes. For further expansion, pellets were gently disrupted with a 10 ml pipette, and the colony suspension was transferred to an inactivated MEFs layer; for 3D seeding, the pellet was rigorously pipetted to obtain single-cell suspensions. For expansion, hiNSCs colonies were seeded from 1 dish into 20 (15cm^2).

Human primary astrocytes. Human primary astrocytes (Sciencell research laboratories, cat. no. 1800) were expanded on 20 µg/mL poly-L-lysine (Sigma, P4832) coated surfaces up to passage 5 following established protocols from the manufacturer. Astrocytes were maintained in astrocyte media supplemented with astrocyte growth factors (1%), Fetal Bovine Serum (2%), and Anti-Anti (1%) from Sciencell research laboratories (cat.no. 1801); media was changed every 3 days. In brief, when astrocytes were 70–80% confluent, they were lifted from the plate via incubation in 0.25% Trypsin/EDTA for 3 min at 37 °C, followed by quenching with complete astrocyte media. Next, the cell suspension was collected from the plates and pelleted by centrifugation at 1,000 rpm for 5 minutes. Cells were re-seeded at 350,000 cells/cm^2.

HMC3 microglia cell line. The HMC3 microglia cell line was obtained from ATCC and maintained following established protocols [46]. In brief, microglia were expanded in 15 cm^2 dishes in EMEM media (ATCC) supplemented with 10% Fetal Bovine Serum (Invitrogen), and 1% Anti-Anti (Invitrogen). The media was changed every 3 days. When cells reached 70-80% confluency, they were lifted from plates with 0.25% Trypsin/EDTA incubation for 3 min at 37 °C. After quenching with microglia complete media, cells were pelleted with centrifugation at 1000 rpm for 5 min. Cells were seeded at 350,000 cells/cm^2.

Induced pluripotent stem cells. The hiPSC line ND41866*C was obtained from the Coriell Biorepository (Camden, NJ, USA). The YZ1 hiPSC line was obtained from Guisepena Tesco courtesy of the University of Connecticut-Wesleyan Stem Cell Core (UCSCC, Farmington, CT, USA). YZ1 cell line is derived from healthy female lung fibroblasts, and the ND41866*C cell line is derived from healthy male skin fibroblasts.

Induced pluripotent stem cells derived microglia. Two iPSC lines from healthy donors (YZ1 and ND418664) were differentiated into microglia following a previously established protocol [26, 27]. iPSCs were expanded in colonies on a Matrigel layer in mTeSR1 Embryonic stem cell media (StemCell Technologies, cat.no. 85850) as directed by batch instructions from the manufacturer. Each differentiation round required one vial of frozen iPSCs. The iPSCs were thawed and incubated in mTeSR1 media supplemented with 0.5 µM Rock Inhibitors (StemCell Technologies, cat.no. 72304) for 24 h at 37 °C, with daily media changes until iPSC colonies were near each another. To lift the colonies, 2 mL of ReLeSR (StemCell Technologies, cat.no. 05872) solution was applied for 30 seconds at room temperature, followed by 3 min of incubation at 37 °C after the ReLeSR was aspirated. Media was added to the plates and the side of the plates was gently tapped to detach the cells. After collecting and centrifuging the cells at 300x *g* for 5 minutes, the cells were split into a 1:6 ratio and re-plated in mTeSR1 media. The following day, the mTeSR1 media was replaced with E8 media (StemCell Technologies, cat.no. 05990), preferable for microglia differentiation. A second splitting followed the same passaging protocol summarized above, following the addition of the E8 media at least once before differentiation.

To initiate iPSC differentiation to hematopoietic stem cells, the iPSCs were seeded in 6-well plates coated in phenol-red free Matrigel with hematopoietic differentiation media (StemCell Technologies, cat.no. 05310). The media was changed following the manufacturer's protocol. After 11 days, early progenitors of hematopoietic cells were collected and counted and then seeded in 6-well plates coated with phenol-red free Matrigel (~ 400,000 cells/well); 2 mL of microglia differentiation media composed of DMEM-F12 phenol red-free media supplemented with 2% B-27 and 0.5% N2 supplements, 1% Glutamax, 5 µg/mL Insulin, 2% Insulin-Transferin-Selenite, 1% Non-essential amino acids, and 400 µM monothioglycerol was added to each well with freshly infused 100 ng/mL interleukin- 34 (IL-34), 25 ng/mL macrophage colony-stimulating factor (MCSF), and 50 ng/mL transforming growth factor beta (TGFβ) growth factors. Then 1 ml of fresh media was supplemented with IL-34 (R&D systems, cat. No. 5265-IL-010), MCSF (Invitrogen, cat.no. PHC9501), and TGFβ (Fisher, cat.no. 5018578) growth factors every other day. On days 12 and 24 of growth, 5 mL of the 6 mL of media in each well was removed and centrifuged to remove the media with accumulated waste. The cells were resuspended in 1 mL of media and replated into the respective well. On day 25 of growth, the media was supplemented with 100 ng/mL fractalkine (Invitrogen, cat.no. 10636H08H50) and 100 ng/mL OX-2 membrane glycoprotein (CD200) (R&D systems, cat.no. 27712CD050) growth factors in addition to the previously described growth factors.

Hematopoietic stem cells and iPSC-derived microglia were characterized for cell-specific marker expression after each round of differentiation. Live cells were stained with a panel of markers: clusters of differentiation 43, 34, 235, 41, 45, 117 (CD43, CD34, CD235, CD41, CD45, c-kit), triggering receptor expressed on myeloid cells 2 (TREM2), transmembrane protein 119 (TMEM119), and C-X3-C motif chemokine receptor 1 (CX3CR1) and imaged with a Leica SP8 Confocal microscope (Leica Microsystems).

3D in vitro human triculture brain tissue model fabrication. The system for generating 3D human tricultures was modified from our earlier published protocols of 3D rat, mouse, and human neuronal monocultures [17, 47, 48]. When hiNSCs, primary astrocytes, and HMC3s reached nearly 100% confluency, they were collected and pelleted as described in the individual culture methods and then combined to achieve the following ratio: 2:0.5:0.1 million neurons, astrocytes, and microglia, respectively. The same ratio was used for cocultures for the respective cell types. Immediately before seeding the triculture cell solution, previously prepared PLO- and laminin-coated silk scaffolds were placed in 96-well plates, and a vacuum manifold was used to remove excess liquid. Calculations were performed so that each 40µL of cell suspension contained 2:0.5:0.1 million neurons, astrocytes, and microglia. Then 40µL of the cell suspension was pipetted onto the semi-dried scaffolds and incubated for 30 minutes at 37 °C to allow the cells to attach. After this, 150µL of Neuronal media was added to each well. Neuronal media was composed of NeuroBasal medium supplemented with 2% B-27, 1% Anti-Anti, 1% Glutamax, and 1% astrocytes growth factors. The scaffolds were placed in a tissue culture incubator (37 °C, 5% CO_2 in a humidified atmosphere). The following day, the cell-seeded scaffolds were transferred to new 96-well plates. To each scaffold, 100µL of collagen type I solution (Corning or R&D systems, 3 mg/mL with a pH adjusted to 7.0-7.2 with NaOH) was added and then incubated for 30 minutes at 37 °C to allow the collagen gel to crosslink. Next, 150µL of neural media was added to all scaffolds and incubated for 24 h at 37 °C. The following day, the brain-like tissues were moved into 48-well plates with 1 ml of Neuronal media in each well. Media was changed

every fourth day until the tissues were used for injury studies, as controls, or for analysis 6 weeks after seeding.

3D model injury and drug treatment

Contusion injury (controlled cortical impact model (CCI)). At six weeks, the 3D brain-like tissues were placed on a flat weigh boat and subjected to contusion injury using a pneumatic cylinder with a 3 mm flat tip impactor at a velocity of 6 m/s, penetration depth 0.6 mm, and a dwell time duration of 200 ms [17]. Sham tissues were handled similarly to the injured tissues but without receiving the contusion injury. Following injury or sham protocol, the tissues were incubated at 37 °C in 5% CO_2 in a humidified atmosphere until the indicated time marks for analysis of lactate dehydrogenase (LDH) and glutamate release in the medium, cell death, neural network stricture, western blot, and mitochondria health.

Drug treatment. Dynamin-related protein 1 (Drp1) – mitochondria fission 1 protein (Fis1) peptide inhibitor P110 was purchased from Tocris Bioscience (cat. No.68971) [16]. For each independent experiment, a new vial of P110 was freshly reconstituted in deionized water at 1 mg/mL. Immediately following injury or sham treatment, tissues were treated with either 2.4μL of a) P110 (reconstituted) to achieve 1 μM concentration or b) control treatment (deionized water). Tissues were then incubated at 37 °C in 5% CO_2 and a humidified atmosphere until the indicated time marks for analysis of LDH and glutamate release in the medium, cell death, neural network structure, protein expression, and mitochondrial health.

Cell health and TBI progression analysis

Lactate dehydrogenase activity assay. The cellular viability of the brain-like tissues was tested using a lactate dehydrogenase assay (LDH) (Sigma, cat.no. MAK066-1KT) following the manufacturer's protocol. LDH assays measure LDH activity via 1,4-dihydro nicotinamide adenine dinucleotide (NADH) formation from nicotinamide adenine dinucleotide (NAD). Cell culture media was collected at the indicated experimental time points and stored at −80 °C until all media samples were ready for analysis. Then, 50 µl of LDH assay supernatant was added to each sample, and the NADH levels were read with a SpectraMax M3 TECAN plate reader at 450 nm. LDH activity was calculated in the following three steps: a) a calibration curve was generated for each individual plate read from standards; b) absorbances were compared to the calibration curve to calculate NADH levels; c) LDH activity was based on the reaction time and the applied dilution.

Glutamate assay. Free glutamate in the media was measured with a Glutamate assay kit (Abcam, cat.no ab83389) following the manufacturer's protocol. Cell culture media was collected at the indicated experimental time points and stored at −80 °C until analysis. Then 50 µl of sample supernatant and 50 µl of glutamate reaction mix (enzyme mix) were combined. The reaction between the enzyme mixture and glutamate substrate was measured with a SpectraMax M3 TECAN plate reader at 450 nm. Calibration curves were generated from standards for each individual plate. Glutamate concentrations were derived via comparison to the calibration curve.

Viability staining. 3D tissue viability was checked at 2 and 6 weeks after seeding following the established Calcein AM (Invitrogen, C1430) staining protocol. In brief, scaffolds were transferred to clean 48 well plates prior to staining, and 300-500 µl of 2 µM Calcein AM solution was added to each 3D tissue. The samples were then incubated for 30 minutes at 37 °C in the dark. When 30 minutes passed, samples were immediately moved for imaging with Leica SP8 Confocal at 37 °C using 494/517 nm excitation/emission wavelengths.

Immunofluorescence staining and analysis. A solution composed of 4% sucrose and 4% paraformaldehyde (PFA, Electron Microscopy Sciences) in PBS was used to fix the 3D brain-like tissues. After fixing, the tissues were washed five times with PBS and then permeabilized for 1 h with 0.2% TritonX-100 supplemented with 4% goat serum (Thermo Fisher). The permeabilization solution was also used to generate a primary antibody solution. Tissues were incubated in the primary antibody at 4 °C overnight, then washed with gentle shaking in PBS five times (5 minutes each wash). After washes, tissues were incubated with secondary antibodies diluted in PBS for 1 hour. 4′,6-Diamidino-2-Phenylindole (DAPI) was applied to the tissues for 5 min following secondary antibody staining. Five additional PBS washes were used to dispose of any unbound antibodies or DAPI. For all figures, fluorescent image stacks of the stained 3D brain-like tissues were acquired on a Leica SP8 FLIM confocal microscope (Leica Microsystems, Fluotar VISIR 40x/0.95 WATER objective, 290.62 µm x 290.62 µm x 41.81 µm, each maximum projection had 100 z-steps with 0.422 µm in depth each). Images in the figures represented maximum intensity projection and were collected with the same PMT gain settings and laser power between at least three independent experiments. Tuj1 neuronal network density was analyzed using a custom MATLAB code published earlier in our group [17].

Primary antibodies included: anti-TOMM20 (ab186735 rabbit; 1:1000); anti-TOMM20 (ab56783 mouse; 1:1000); anti-beta-tubulin III (ab18207 rabbit; 1:1000); anti-beta-tubulin III (ab78078 mouse; 1:1000); purchased from Abcam.

Secondary antibodies included: goat anti-mouse IgG1, IgG2 (A-21240, A21135), anti-rabbit (A11037) or anti-chicken (A21449) Alexa 488 and 568, 647 (1:500; Thermo); goat anti-chicken (A10040) Alexa 546 (1:500; Life Technologies).

Mitochondria aspect ratio analysis. The ratio of mitochondria length vs. width (Aspect ratio) was measured using available macro from NIH ImageJ software, following the published protocol [49]. In brief, maximum projection images of TOMM20-positive mitochondria, acquired with Leica SP8 confocal (1024 ×1024 pixels, Fluotar VISIR 40x/0.95 WATER objective), were analyzed by ImageJ Marco. The measured AR for each mitochondrion in at least four images (individual samples) was plotted as a distribution graph for comparison with other groups.

Western blot. To extract cellular protein lysate, entire scaffolds previously frozen at -80 °C were incubated in 1X RIPA lysis buffer (Sigma, 20-188) supplemented with a protease and phosphatase inhibitor cocktail (Invitrogen, A32961) and sonicated at 20% amplitude for 20 pulses (1 second on, 1 second off). According to the manufacturer's instructions, the protein concentration was quantified at a 1:200 dilution using a Bradford assay (Invitrogen, 23200).

For the analysis, 5 µg of extracted protein was separated on a 4-12% Bolt Bis-Tris gel (Invitrogen, NW04125BOX) and transferred using an iBlot2 Transfer system (Invitrogen) to PVDF membranes (Invitrogen, IB242002) at 23 V for 3 minutes. Membranes were blocked for 30 minutes at room temperature in 5% BSA or 5% non-fat dry milk (NFDM) (Jackson Immuno Research Labs, 001-000-161) in TBST (Boston BioProducts, IBB-181) and then incubated with primary antibodies diluted in 5% BSA or NFDM at 4 °C overnight on a rocker. To remove excess antibodies, the membranes were washed twice in TBST, followed by 3 10-minute washes at 4 °C. The membranes were then incubated in a secondary antibody solution for 1 h in 5% BSA or NFDM at 4 °C. Following three 10-minute washes at 4 °C, the membranes were incubated for 5 minutes in the dark with SuperSignal™ West Pico Plus substrate ((Invitrogen, 34577) used for actin and Tuj1 detection) or SuperSignal™ West Atto Ultimate Sensitivity substrate ((Invitrogen, A38555) used for detection of the rest of the proteins) to identify the proteins of interest. The membranes were serially imaged using a BioRad ChemiDoc MP. The images were analyzed using ImageJ Software.

Primary antibodies included: anti-DRP1 (ab184247 rabbit; 1:1000); anti-Fis1 (ab156865 rabbit; 1:1000); anti-MAP2 (ab5392 rabbit; 1:10000); anti-TOMM20 (ab186735 rabbit; 1:1000); anti-TOMM20 (ab56783 mouse; 1:1000); anti-beta-tubulin III (ab18207 rabbit; 1:1000); anti-beta-tubulin III (ab78078 mouse; 1:1000); anti-VDAC1 (ab154856 rabbit; 1:1000); anti-mitochondrial (ab92824 mouse; 1:1000); anti-actin HRP conjugated (ab20272 mouse; 1:1000); purchased from Abcam, and anti-DRP1 (phosphor S616) (3455 S rabbit; 1:1000) purchased from Cell Signal Technologies.

Secondary antibodies purchased from Cell Signal Technologies included: HRP – conjugated (anti-rabbit IgG 7074P2; anti-mouse IgG 7076 S).

Protein array – cytokine panel. For the production level of 30 proteins associated with the neuronal state in health and disease, we used the Human Neuro Discovery Array (AAH-NEU-2-8, Ray Biotech) following the manufacturer's protocol. In brief, 1 ml of conditioned media (pooled from 3 independent samples) was used per one membrane, with 3-4 total samples per condition (Sham and CCI, P110 untreated/treated), each from one independent experiment. The membranes were imaged using a BioRad ChemiDoc MP. The images were analyzed using ImageJ Software following the manufacturer's instructions. Data were normalized first to internal controls in each array and then to arrays performed on a sham group without drug treatment in parallel to the injured +/- P110 groups and the P110 sham group. The presented data is the CCI (contusion injury) ratio over Sham (untreated).

Mitochondria isolation and treatment of 3D in vitro brain cultures. Mitochondria isolation and transfer experiments were conducted following established protocols [14]. In brief, the media from 3D in vitro cultures (neurons, microglia, or astrocytes – depending on the experimental set-up) was collected into the 1.5 ml Eppendorf tubes and centrifuged for 10 minutes at 1000x *g* to pellet the nuclei. The post-nuclear supernatant was centrifuged at 13,000x *g* for 25 minutes to collect a mitochondria-enriched fraction. After mitochondria pellets were generated, the mitochondria were reconstituted in 100 µl of neuronal medium and transferred to 900 µl of media in naïve scaffolds seeded with neurons, microglia, or astrocytes (depending on the experimental set-up) for 24 h of incubation. The treatment groups received a fresh dose of the P110 peptide at each transfer step. The residual mitochondria-free media after centrifugation was stored at -20 °C for LDH and Glutamate release analysis. Isolated mitochondria were characterized for mitochondria-specific markers expression: mitochondria, TOMM20, and VDAC1 (Supplementary Fig. 14a-b).

RNA Isolation Protocol

Scaffolds were collected and stored at -80˚C. Upon isolation, samples were thawed on ice and incubated with 600 µL of Lysis Buffer from RNeasy Kit (Qiagen, Catalog No. 74106). During incubation, samples were cut up using small scissors and continued to sit in a lysis buffer for approximately 20 minutes. The lysed samples were placed onto QIAshredder Mini Spin (Qiagen) columns and spun at 10,000 rpm for 2 minutes. An equal amount of 70% ethanol was added to the supernatant and mixed thoroughly. The ethanol-containing mixture was spun in two rounds through the RNeasy Mini Spin column (Qiagen) at 10,000 rpm for 1 minute each; the flow through was discarded. In a new collection tube, 400 µL of RNA wash from SurePrep RNA/DNA/Protein Purification Kit (Fisher Scientific, Catalog No. BP2802-50) was added to the RNeasy column and spun at the same setting for 1 minute; the flow through was discarded. After the first RNA Wash, 30 µL of DNase and RDD buffer (1:7 ratio) containing solution from the RNase-Free DNase Set (Qiagen, Catalog No. 79254) was incubated on the columns at room temperature for 15 minutes before a second and third round of RNA was performed as well as a final spin to ensure the column was dry. The column was placed into a 1.5 mL microcentrifuge tube, and 22uL of RNA Elution Solution (Fisher Scientific) was added to the center of the column and spun at 12,000 rpm for 1 minute. Samples were then read on the NanoDrop 2000 spectrophotometer and stored at -80˚C before sequencing.

Messenger RNA (mRNA) sequencing and bioinformatic analysis

Approximately 1 µg of total RNA for each sample underwent RNA quality control analyses before library preparation and bulk mRNA sequencing, as previously described [50, 51]. RNA integrity numbers (RIN) were determined with a Bioanalyzer 2100 (Agilent Technologies, Santa Clara, CA, USA), which indicated minimal RNA degradation. Illumina Novaseq sequencers generated paired-end reads (150 bp) at a read depth of 20 million reads [50].

Raw sequencing reads (.fastq files) were uploaded to the Tufts University Galaxy Server [52] for analysis, first utilizing FastQC (https://www.bioinformatics.babraham.ac.uk/) for quality control before reading alignment with RNA STAR [53] (reference genome GRCh38.p13, https://www.ncbi.nlm.nih.gov/) and quantification using featureCounts [54]. Differentially expressed gene lists were created using the DESeq2 R package [55] by comparing injury and Sham conditions, with or without P110 treatment. Gene set enrichment analyses (GSEA) were performed using the desktop software (https://www.gsea-msigdb.org/gsea/index.jsp) [56, 57] using MitoCarta3.0 [58] and custom curated mitochondrial pathway [59] databases. Heatmaps were generated using the pheatmap R package. Gene module co-expression analyses were performed with the CEMiTool R package [60, 61], GSEA using the Reactome pathway database (https://reactome.org/), and signed interaction network analysis utilizing high confidence STRING protein-protein interactions (STRING score > 700).

Metabolic imaging and Data analysis

Images were acquired using a Leica TCS SP8 confocal microscope equipped with a tunable (680 to 1300 nm) femtosecond laser (InSight Deep See; Spectra-Physics; Mountain View, California) and a water-immersion 40× objective (NA 1.1). Two-photon excited fluorescence (TPEF) images (1024 ×1024 pixels, 290.6 ×290.6 µm) were acquired at 755 nm excitation and two emission ranges at 460 ± 25 nm and 525 ± 25 nm. Location co-registered NAD(P)H lifetime data were then acquired at the same excitation and emission wavelengths with a 1-minute integration time (512 ×512 pixels) using a Picoquant Picoharp 300 time-correlated single photon counter and SymPhoTime analysis software. A three-level Otsu's threshold and a combination of two-dimensional (2D) discrete Fourier transform and power spectral density (PSD) methods were applied to binarized images to segment out the mitochondria regions [62]. 2D pixel-wise redox ratio maps were generated based on the fluorescence intensities from two different emission channels with the expression of 1, 2, with the 525 nm channel for FAD fluorescence and the 460 nm channel for NAD(P)H fluorescence.

$$Redox\ ratio_{(i,j)} = \frac{FAD_{(i,j)}}{FAD_{(i,j)} + NAD(P)H_{(i,j)}} \quad (1)$$

$$\begin{aligned} NADH_{adj} &= \gamma(C_{460em} - 0.0101 * C_{525em}); FAD_{adj} \\ &= \gamma(C_{525em} - 0.6699 * C_{460em} * 0.15) \end{aligned} \quad (2)$$

Lifetime data were saved into 261-time bins with equal intervals (12.5 ns in length) and processed using a phasor approach as previously described [63]. Briefly, this approach does not require prior knowledge of the fluorophores within the samples. It has a high sensitivity to environmental perturbations and can provide complementary information on the nature of fluorophores to the intensity data. In this study, we introduced a phasor-guided redox ratio distribution analytical approach, where we considered the redox ratio from NAD(P)H-containing pixels by mapping the location of specific regions of the phasor distribution data to the original lifetime images and then to the co-registered pixels in the NAD(P)H and FAD intensity images. After Fourier transformation, the pixel-wise lifetime information was converted to a set of g and s cos and sin components, respectively. The redder hues in the phasor map represent more pixels with similar frequency components, while the bluer hues have fewer ones (Fig. 5h and Supplementary Figures 34-35). A linear fit was applied to all the g and s phasor values corresponding to the lifetime spectra from all pixels of a field. The two points where the line intersected the universal semicircle represented the short and long NAD(P)H lifetimes; the bound NAD(P)H fraction was estimated based on the projected location of each phasor point on the fitted line, according to the equation 3 as shown in Supplemental Fig. 23 [63].

$$Bound\ fraction = \frac{MS}{LS} \quad (3)$$

The pixel-wise redox ratio values were extracted by mapping back the NAD(P)H phasor locations to the original 2D images and referring to the co-registered NADH and FAD intensity images. All redox values from each sample were sorted into 10 bins ranging from 0 to 1, with 0.1 intervals. A metric AUC ratio, calculated according to equation 3, was used to quantify the redox distribution differences among different treatment groups (CCI vs. Sham, P110 CCI vs. P110 Sham).

$$AUC\ ratio = \frac{\text{AUC within } 0.4 - 0.9 \text{ range}}{\text{AUC within } 0.1 - 0.4 \text{ range}} \quad (4)$$

Region selection: Autofluorescence lifetime spectra from all the samples of this study were mapped into four main regions of the phasor space (Supplementary Fig. 34). Data within the heavily overlapped Q1 and Q2 regions were present in all fields and accounted for most of the pixels (> 95%, Supplementary Fig. 36G), while lifetime spectra that were mapped within the Q3 and Q4 regions could only be occasionally detected with varying prevalence. Redox distributions from the Q1, Q2, and overlapped regions were almost identical (Supplementary Fig. 34 F), indicating they may correspond to NADH and NADPH [64]. The redox ratio distributions of the pixels mapped to the Q3 and Q4 phasor spaces were more right-shifted, indicating a distinct origin, possibly from the retinol and retinoic acids [65]. Therefore, to avoid artifacts introduced by other fluorophores besides NAD(P)H, redox analysis in this study focused on pixels with lifetime spectra mapped within the Q1, Q2, and their overlapped regions.

All the intensity images were power and detector gain normalized before analysis according to equation 5. Incident power was measured with a power meter before every experiment session before the objective.

$$Normalized\ intensity\ image = \frac{Raw\ intensity\ image}{Detector\ gains * Incident\ power^2} \quad (5)$$

Two cell lines, HMC3, and iPSCs-derived microglia, each with two independent rounds, three dependent transfers, and four treatment conditions, were imaged. For each treatment, 2-4 samples with 3-4 locations were acquired. In total, for each cell line, results were from at

least 5 samples from each treatment condition (N_{Sham} = 5-6, $N_{P110,\ Sham}$ = 5-6,$N_{P110,\ CCI}$ = 7-8,$N_{P110,\ Sham}$ = 7-8). All the CCI (contusion injury) data were normalized to corresponding shams.

Statistical analysis. Statistical analysis was performed between and within experimental groups using GraphPad Prism 9 software. Two-tailed t-tests were used to compare values within an experimental group and between two experimental groups. One- or two-way ANOVA analysis of variance was used to compare multiple groups. Tukey's post hoc tests were used to assess computed significant differences between experimental and control groups. Any *p*value less than 0.05 was considered statistically significant. Each experiment was repeated at least three times; technical replicates (2-6, depending on the experiment) were used for every assay. Quantified data graphically presented the mean and standard error of the mean (SEM) of each group. The sample size was chosen based on the power analysis of previously conducted experiments with in vitro brain tissue cultures.

DATA AVAILABILITY

All data generated or analyzed during this study are included in this article (and its supplementary information files). This study's mRNA sequencing data set was deposited to the GEO repository database (https://www.ncbi.nlm.nih.gov/geo/) with accession number GSE237013.

REFERENCES

1. Jassam YN, Izzy S, Whalen M, McGavern DB, El Khoury J. Neuroimmunology of Traumatic Brain Injury: Time for a Paradigm Shift. Neuron 2017;95:1246–65.
2. Ladak AA, Enam SA, Ibrahim MT. A Review of the Molecular Mechanisms of Traumatic Brain Injury. World Neurosurg. 2019;131:126–32.
3. Burda JE, Bernstein AM, Sofroniew MV. Astrocyte roles in traumatic brain injury. Exp Neurol. 2016;275:305–15. Pt 3
4. Crotti A, Ransohoff RM. Microglial Physiology and Pathophysiology: Insights from Genome-wide Transcriptional Profiling. Immunity 2016;44:505–15.
5. Loane DJ, Kumar A. Microglia in the TBI brain: The good, the bad, and the dysregulated. Exp Neurol. 2016;275:316–27. Pt 3
6. Zhou Y, Shao A, Yao Y, Tu S, Deng Y, Zhang J. Dual roles of astrocytes in plasticity and reconstruction after traumatic brain injury. Cell Commun Signal. 2020;18:62.
7. Chen Y, Swanson RA. Astrocytes and brain injury. J Cereb Blood Flow Metab. 2003;23:137–49.
8. Henry RJ, Ritzel RM, Barrett JP, Doran SJ, Jiao Y, Leach JB, et al. Microglial Depletion with CSF1R Inhibitor During Chronic Phase of Experimental Traumatic Brain Injury Reduces Neurodegeneration and Neurological Deficits. J Neurosci. 2020;40:2960–74.
9. Bader V, Winklhofer KF. Mitochondria at the interface between neurodegeneration and neuroinflammation. Semin Cell Dev Biol. 2020;99:163–71.
10. Herst PM, Rowe MR, Carson GM, Berridge MV. Functional Mitochondria in Health and Disease. Front Endocrinol (Lausanne). 2017;8:296.
11. Norat P, Soldozy S, Sokolowski JD, Gorick CM, Kumar JS, Chae Y, et al. Mitochondrial dysfunction in neurological disorders: Exploring mitochondrial transplantation. NPJ Regen Med. 2020;5:22.
12. Liddelow SA, Guttenplan KA, Clarke LE, Bennett FC, Bohlen CJ, Schirmer L, et al. Neurotoxic reactive astrocytes are induced by activated microglia. Nature 2017;541:481–7.
13. Hernandez-Ontiveros DG, Tajiri N, Acosta S, Giunta B, Tan J, Borlongan CV. Microglia activation as a biomarker for traumatic brain injury. Front Neurol. 2013;4:30.
14. Joshi AU, Minhas PS, Liddelow SA, Haileselassie B, Andreasson KI, Dorn GW 2nd, et al. Fragmented mitochondria released from microglia trigger A1 astrocytic response and propagate inflammatory neurodegeneration. Nat Neurosci. 2019;22:1635–48.
15. Wu Q, Gao C, Wang H, Zhang X, Li Q, Gu Z, et al. Mdivi-1 alleviates blood-brain barrier disruption and cell death in experimental traumatic brain injury by mitigating autophagy dysfunction and mitophagy activation. Int J Biochem Cell Biol. 2018;94:44–55.
16. Qi X, Qvit N, Su YC, Mochly-Rosen D. A novel Drp1 inhibitor diminishes aberrant mitochondrial fission and neurotoxicity. J Cell Sci. 2013;126:789–802. Pt 3
17. Liaudanskaya V, Chung JY, Mizzoni C, Rouleau N, Berk AN, Wu L, et al. Modeling Controlled Cortical Impact Injury in 3D Brain-Like Tissue Cultures. Adv Health Mater. 2020;9:e2000122.
18. Wu L, Chung JY, Cao T, Jin G, Edmiston WJ 3rd, Hickman S, et al. Genetic inhibition of RIPK3 ameliorates functional outcome in controlled cortical impact independent of necroptosis. Cell Death Dis. 2021;12:1064.
19. Poyhonen S, Er S, Domanskyi A, Airavaara M. Effects of Neurotrophic Factors in Glial Cells in the Central Nervous System: Expression and Properties in Neurodegeneration and Injury. Front Physiol. 2019;10:486.
20. Gyoneva S, Ransohoff RM. Inflammatory reaction after traumatic brain injury: therapeutic potential of targeting cell-cell communication by chemokines. Trends Pharm Sci. 2015;36:471–80.
21. Daoud H, Alharfi I, Alhelali I, Charyk Stewart T, Qasem H, Fraser DD. Brain injury biomarkers as outcome predictors in pediatric severe traumatic brain injury. Neurocrit Care. 2014;20:427–35.
22. Yan EB, Satgunaseelan L, Paul E, Bye N, Nguyen P, Agyapomaa D, et al. Post-traumatic hypoxia is associated with prolonged cerebral cytokine production, higher serum biomarker levels, and poor outcome in patients with severe traumatic brain injury. J Neurotrauma. 2014;31:618–29.
23. Goyal A, Failla MD, Niyonkuru C, Amin K, Fabio A, Berger RP, et al. S100b as a prognostic biomarker in outcome prediction for patients with severe traumatic brain injury. J Neurotrauma. 2013;30:946–57.
24. Woodcock T, Morganti-Kossmann MC. The role of markers of inflammation in traumatic brain injury. Front Neurol. 2013;4:18.
25. Quinn KP, Sridharan GV, Hayden RS, Kaplan DL, Lee K, Georgakoudi I. Quantitative metabolic imaging using endogenous fluorescence to detect stem cell differentiation. Sci Rep. 2013;3:3432.
26. Abud EM, Ramirez RN, Martinez ES, Healy LM, Nguyen CHH, Newman SA, et al. iPSC-Derived Human Microglia-like Cells to Study Neurological Diseases. Neuron 2017;94:278–93 e9.
27. McQuade A, Coburn M, Tu CH, Hasselmann J, Davtyan H, Blurton-Jones M. Development and validation of a simplified method to generate human microglia from pluripotent stem cells. Mol Neurodegener. 2018;13:67.
28. Virmani MA, Cirulli M. The Role of l-Carnitine in Mitochondria, Prevention of Metabolic Inflexibility and Disease Initiation. Int J Mol Sci. 2022;23:2717.
29. Weber B, Lackner I, Haffner-Luntzer M, Palmer A, Pressmar J, Scharffetter-Kochanek K, et al. Modeling trauma in rats: similarities to humans and potential pitfalls to consider. J Transl Med. 2019;17:305.
30. Whalen MJ, Dalkara T, You Z, Qiu J, Bermpohl D, Mehta N, et al. Acute plasmalemma permeability and protracted clearance of injured cells after controlled cortical impact in mice. J Cereb Blood Flow Metab. 2008;28:490–505.
31. Glushakov AV, Robbins SW, Bracy CL, Narumiya S, Doré S. Prostaglandin F2α FP receptor antagonist improves outcomes after experimental traumatic brain injury. J Neuroinflammation. 2013;10:1–14.
32. Hinzman JM, Wilson JA, Mazzeo AT, Bullock MR, Hartings JA. Excitotoxicity and Metabolic Crisis Are Associated with Spreading Depolarizations in Severe Traumatic Brain Injury Patients. J Neurotrauma. 2016;33:1775–83.
33. Jalloh I, Carpenter KL, Helmy A, Carpenter TA, Menon DK, Hutchinson PJ. Glucose metabolism following human traumatic brain injury: methods of assessment and pathophysiological findings. Metab Brain Dis. 2015;30:615–32.
34. Watts ME, Pocock R, Claudianos C. Brain Energy and Oxygen Metabolism: Emerging Role in Normal Function and Disease. Front Mol Neurosci. 2018;11:216.
35. Ragan DK, McKinstry R, Benzinger T, Leonard JR, Pineda JA. Alterations in cerebral oxygen metabolism after traumatic brain injury in children. J Cereb Blood Flow Metab. 2013;33:48–52.
36. Di Pietro V, Lazzarino G, Amorini AM, Signoretti S, Hill LJ, Porto E, et al. Fusion or Fission: The Destiny of Mitochondria In Traumatic Brain Injury of Different Severities. Sci Rep. 2017;7:9189.
37. Hayakawa K, Esposito E, Wang X, Terasaki Y, Liu Y, Xing C, et al. Transfer of mitochondria from astrocytes to neurons after stroke. Nature 2016;535:551–5.
38. Borst K, Schwabenland M, Prinz M. Microglia metabolism in health and disease. Neurochem Int. 2019;130:104331.
39. Lauro C, Limatola C. Metabolic Reprograming of Microglia in the Regulation of the Innate Inflammatory Response. Front Immunol. 2020;11:493.
40. Lynch MA. Can the emerging field of immunometabolism provide insights into neuroinflammation? Prog Neurobiol. 2020;184:101719.
41. Wei Y, Wang R, Teng J. Inhibition of Calcium/Calmodulin-Dependent Protein Kinase IIalpha Suppresses Oxidative Stress in Cerebral Ischemic Rats Through Targeting Glucose 6-Phosphate Dehydrogenase. Neurochem Res. 2019;44:1613–20.
42. Rouleau N, Cantley WL, Liaudanskaya V, Berk A, Du C, Rusk W, et al. A Long-Living Bioengineered Neural Tissue Platform to Study Neurodegeneration. Macromol Biosci. 2020;20:e2000004.
43. Liaudanskaya V, Jgamadze D, Berk AN, Bischoff DJ, Gu BJ, Hawks-Mayer H, et al. Engineering advanced neural tissue constructs to mitigate acute cerebral inflammation after brain transplantation in rats. Biomaterials 2019;192:510–22.
44. Rouleau N, Bonzanni M, Erndt-Marino JD, Sievert K, Ramirez CG, Rusk W, et al. A 3D Tissue Model of Traumatic Brain Injury with Excitotoxicity That Is Inhibited by Chronic Exposure to Gabapentinoids. Biomolecules 2020;10:1196.

45. Cairns DM, Chwalek K, Moore YE, Kelley MR, Abbott RD, Moss S, et al. Expandable and Rapidly Differentiating Human Induced Neural Stem Cell Lines for Multiple Tissue Engineering Applications. Stem Cell Rep. 2016;7:557–70.
46. HMC3 CRL-3304 2021 [cited 2021 November 5th]. Available from: https://www.atcc.org/products/crl-3304#detailed-product-information.
47. Tang-Schomer MD, White JD, Tien LW, Schmitt LI, Valentin TM, Graziano DJ, et al. Bioengineered functional brain-like cortical tissue. Proc Natl Acad Sci USA. 2014;111:13811–6.
48. Sood D, Cairns DM, Dabbi JM, Ramakrishnan C, Deisseroth K, Black LD 3rd, et al. Functional maturation of human neural stem cells in a 3D bioengineered brain model enriched with fetal brain-derived matrix. Sci Rep. 2019;9:17874.
49. Valente AJ, Maddalena LA, Robb EL, Moradi F, Stuart JA. A simple ImageJ macro tool for analyzing mitochondrial network morphology in mammalian cell culture. Acta Histochem. 2017;119:315–26.
50. Fiore NJ, Ganat YM, Devkota K, Batorsky R, Lei M, Lee K, et al. Bioengineered models of Parkinson's disease using patient-derived dopaminergic neurons exhibit distinct biological profiles in a 3D microenvironment. Cell Mol Life Sci. 2022;79:78.
51. Fiore NJ, Tamer-Mahoney JD, Beheshti A, Nieland TJF, Kaplan DL. 3D biocomposite culture enhances differentiation of dopamine-like neurons from SH-SY5Y cells: A model for studying Parkinson's disease phenotypes. Biomaterials 2022;290:121858.
52. Afgan E, Baker D, Batut B, van den Beek M, Bouvier D, Cech M, et al. The Galaxy platform for accessible, reproducible and collaborative biomedical analyses: 2018 update. Nucleic Acids Res. 2018;46:W537–W44. W1
53. Dobin A, Davis CA, Schlesinger F, Drenkow J, Zaleski C, Jha S, et al. STAR: ultrafast universal RNA-seq aligner. Bioinformatics 2013;29:15–21.
54. Liao Y, Smyth GK, Shi W. featureCounts: an efficient general purpose program for assigning sequence reads to genomic features. Bioinformatics 2014;30:923–30.
55. Love M, Anders S, Huber W. Differential analysis of count data–the DESeq2 package. Genome Biol. 2014;15:10.1186.
56. Subramanian A, Tamayo P, Mootha VK, Mukherjee S, Ebert BL, Gillette MA, et al. Gene set enrichment analysis: a knowledge-based approach for interpreting genome-wide expression profiles. Proc Natl Acad Sci USA. 2005;102:15545–50.
57. Mootha VK, Lindgren CM, Eriksson K-F, Subramanian A, Sihag S, Lehar J, et al. PGC-1α-responsive genes involved in oxidative phosphorylation are coordinately downregulated in human diabetes. Nat Genet. 2003;34:267–73.
58. Rath S, Sharma R, Gupta R, Ast T, Chan C, Durham TJ, et al. MitoCarta3.0: an updated mitochondrial proteome now with sub-organelle localization and pathway annotations. Nucleic Acids Res. 2020;49:D1541–D7.
59. Guarnieri JW, Dybas JM, Fazelinia H, Kim MS, Frere J, Zhang Y, et al. Targeted Down Regulation Of Core Mitochondrial Genes During SARS-CoV-2 Infection. bioRxiv. 2022:2022.02.19.481089.
60. Russo PST, Ferreira GR, Cardozo LE, Bürger MC, Arias-Carrasco R, Maruyama SR, et al. CEMiTool: a Bioconductor package for performing comprehensive modular co-expression analyses. BMC Bioinforma. 2018;19:56.
61. Langfelder P, Horvath S. WGCNA: an R package for weighted correlation network analysis. BMC Bioinforma. 2008;9:559.
62. Quinn KP, Bellas E, Fourligas N, Lee K, Kaplan DL, Georgakoudi I. Characterization of metabolic changes associated with the functional development of 3D engineered tissues by non-invasive, dynamic measurement of individual cell redox ratios. Biomaterials 2012;33:5341–8.
63. Liu Z, Pouli D, Alonzo CA, Varone A, Karaliota S, Quinn KP, et al. Mapping metabolic changes by noninvasive, multiparametric, high-resolution imaging using endogenous contrast. Sci Adv. 2018;4:eaap9302.
64. Huang S, Heikal AA, Webb WW. Two-photon fluorescence spectroscopy and microscopy of NAD(P)H and flavoprotein. Biophys J. 2002;82:2811–25.
65. Datta R, Alfonso-Garcia A, Cinco R, Gratton E. Fluorescence lifetime imaging of endogenous biomarker of oxidative stress. Sci Rep. 2015;5:9848.

ACKNOWLEDGEMENTS

The authors thank the NIH (R01AG061838 and P41EB027062), the Department of Defense Technology for the Warfighter Program (HU0001-20-2-0015), the NIH Research Infrastructure grant (NIH S10OD021624) for the purchase of the microscope, Dr. Yu-Ting L. Dingle, of Pipette & Stylus LLC, for assistance with illustrations and figures, Prof. Afshin Beheshti for initial assistance with mRNA sequencing analysis, Dr. Dana Cairns, for supplying hiNSC cells, Rushil Bakhshi for testing the mitochondria isolation protocol. And Dr. Dustin Snapper for help with the discussion of the results. The opinions and assertions expressed herein are those of the authors and do not necessarily reflect the official policy or position of the Uniformed Services University or the Department of Defense.

AUTHOR CONTRIBUTIONS

VL, MJW, AJS, IG, TJFN, and DLK conceived the project, designed, interpreted the experiments, and wrote the manuscript. VL conducted all in vitro experiments. VL isolated mitochondria, YZ Collected metabolic images of mitochondria, YZ and IG performed the analysis. VL, YM, MC, AM, AS-Z. Expanded cells for triculture seeding experiments, VL and MC differentiated and analyzed iPSC-derived microglia with MB-J guidance, MFK, YM, AS-Z performed sample maintenance (media changes). VL, YM, MFK, VKR, and MRS conducted western blots. VL, YM, MFK, VKR, MRS, AB, AS-Z performed biochemical assays, immunofluorescent staining, and with AM fabrication of silk scaffolds. VL collected all immunofluorescent images. VL and MFK performed and analyzed protein arrays. VL and MFK performed mRNA isolation, and NJF performed mRNA sequencing analysis.

COMPETING INTERESTS

The authors declare no competing interests.

ETHICS

This work did not include any experiments with animals or the participation of human subjects.

ADDITIONAL INFORMATION

Supplementary information The online version contains supplementary material available at https://doi.org/10.1038/s41419-023-05980-0.

Correspondence and requests for materials should be addressed to David L. Kaplan.

Reprints and permission information is available at http://www.nature.com/reprints

Publisher's note Springer Nature remains neutral with regard to jurisdictional claims in published maps and institutional affiliations.